

<https://doi.org/10.1038/s41612-024-00662-w>

# Competing impacts of tropical Pacific and Atlantic on Southern Ocean inter-decadal variability

Check for updates

Shuai-Lei Yao <sup>1</sup>✉, Renguang Wu <sup>2</sup>✉, Jing-Jia Luo <sup>3</sup> & Wen Zhou <sup>4</sup>

The observed Southern Ocean sea surface temperature (SST) has experienced prominent inter-decadal variability nearly in phase with the Inter-decadal Pacific Oscillation (IPO), but less associated with the Atlantic Multidecadal Variability (AMV), challenging the prevailing view of Pacific-Atlantic synergistic effects. Yet, the mechanisms of distinct trans-hemispheric connections to the Southern Ocean remain indecisive. Here, by individually constraining the observed cold-polarity and warm-polarity IPO and AMV SSTs in a climate model, we show that the IPO is influential in initiating a basin-wide Southern Ocean response, with the AMV secondary. A tropical Pacific-wide cooling triggers a basin-scale Southern Ocean cold episode through a strong Rossby wave response to the north-to-south cross-equatorial weakened Hadley circulation. By contrast, due to the competing role of tropical Pacific cooling, an Atlantic warming partly cools the Southern Ocean via a weak Rossby wave response to the south-to-north cross-equatorial enhanced Hadley circulation. Conversely, tropical Pacific warming leads to a warm Southern Ocean episode. Our findings highlight that properly accounting for the tropical Pacific SST variability may provide a potential for skillful prediction of Southern Ocean climate change and more reliable estimates of climate sensitivity, currently overestimated by the misrepresented Southern Ocean warming.

The Southern Ocean (SO), as a vital sink of anthropogenic heat and carbon on the Earth<sup>1,2</sup>, has accounted for about 70% and 40% of the global ocean uptake of anthropogenic heat<sup>3,3</sup> and carbon dioxide<sup>4,5</sup>, respectively. It thereby sets the growth rates of global warming and atmospheric carbon levels. Despite rapidly increasing atmospheric CO<sub>2</sub> concentrations since the industrial revolution, the SO sea surface temperature (SST; 50°S-70°S) displays considerable inter-decadal fluctuations (Supplementary Fig. 1), with alternating cooling and warming episodes in various observational datasets<sup>6,7</sup> and paleoclimate reconstructions<sup>8</sup>, in striking contrast to a progressively mounting response to anthropogenic warming under the sixth Coupled Model Inter-comparison Project (CMIP6) historical runs (Supplementary Fig. 1). The CMIP6-projected SO excessive warming produces generally higher climate sensitivity through a stronger low-cloud-SST positive feedback in the SO than previous generations<sup>9,10</sup>, posing a too-hot-model dilemma in the climate community and even an illusion of a looming

1.5 °C warmer world<sup>9,11</sup>. Given the interconnected climate ramifications, there is an urgent socio-economic need to understand the causes of SO SST variability to confirm the validity of near-future climate projections commonly adopted for climate adaptation, mitigation, and resilience options.

Two major hypotheses have been invoked to decipher the satellite-era observed SO SST cooling. One points to an anthropogenic origin, including the accelerated westerly wind-driven equatorward Ekman transport of colder waters in response to stratospheric ozone loss<sup>12-15</sup> (Note that stratospheric ozone concentration has depleted during the late twentieth century and gradually recovered since the turn of the millennium) and GHG increase<sup>16,17</sup>, and the suppressed upwelling of warmer subsurface waters caused by the increased surface freshening via Antarctic ice sheet and shelf meltwater and sea-ice transport under anthropogenic warming<sup>18-21</sup>. Although anthropogenic warming may potentially contribute to recent SO cooling, the incongruence between the observed expansion and

<sup>1</sup>State Key Laboratory of Numerical Modeling for Atmospheric Sciences and Geophysical Fluid Dynamics, Institute of Atmospheric Physics, Chinese Academy of Sciences, Beijing 100029, China. <sup>2</sup>School of Earth Sciences, Zhejiang University, Hangzhou 310058, China. <sup>3</sup>Institute for Climate and Application Research (ICAR)/CIC-FEMD, Nanjing University of Information Science & Technology, Nanjing 210044, China. <sup>4</sup>Key Laboratory of Polar Atmosphere-ocean-ice System for Weather and Climate, Ministry of Education & Department of Atmospheric and Oceanic Sciences & Institute of Atmospheric Sciences, Fudan University, Shanghai 200443, China. ✉e-mail: [yaoshi08@hotmail.com](mailto:yaoshi08@hotmail.com); [renguang@zju.edu.cn](mailto:renguang@zju.edu.cn)

GHG-simulated decline in the Antarctic sea ice<sup>22,23</sup> exemplifies the perplexing Antarctic sea ice paradox<sup>24</sup> in a warming climate. The other highlights the dominance of internal variability, locally forced by the halted Weddell-Sea deep convection of centennial variability inherent in the SO<sup>7,23,25</sup> or remotely influenced by the cold-phase Inter-decadal Pacific Oscillation (IPO)<sup>22,26,27</sup> and the warm-phase Atlantic Multidecadal Variability (AMV)<sup>24,28</sup>. However, the incompatible chronologies of SO internal centennial variability between global climate models and limited observations<sup>7,23,25</sup> inhibit directly quantifying the full extent of observed SO SST internal variability. Additionally, owing to irregularities in the magnitudes and phase transitions of the IPO and the AMV across models<sup>29</sup>, efforts to establish a trans-hemispheric tropical-SO teleconnection in a wider context of historical SO cooling and warming regimes have been hitherto overlooked. Due to the prevalence of the inter-decadal variability in observed SO SSTs, we need to gain deeper insight into what degree the IPO-related and AMV-related SST anomalies contribute to the SO SST inter-decadal variability of alternating warm and cold episodes.

A better approach to remedy the model limitations is to adopt an idealized restoring framework that paces the model with the time-invariant spatial patterns of the IPO and AMV, corresponding to the internally generated component of observed IPO-SST and AMV-SST anomalies. This method is highly beneficial to singling out the trans-hemispheric tropical-SO teleconnections and, more accurately, quantifying the respective roles of IPO and AMV in triggering the SO SST inter-decadal variability (SOIDV). Here, we provide evidence that the IPO is a decisive driver in modulating the SOIDV through the mid-to-high-latitude Rossby wave train, with the AMV playing a smaller role.

## Results

### Observed linkage between the SOIDV and IPO

To objectively determine the observed SOIDV, we apply an empirical orthogonal function (EOF) analysis to the quadratically detrended, 10-year low-pass-filtered annual-mean SST anomalies over the SO domain in five different observational datasets (Methods). We extract the first three dominant modes (all together explaining more than 50% of the total variance in Supplementary Fig. 2) and their corresponding principal components (Supplementary Fig. 3) in each data, with the three modes being well separated. The most dominant mode describes a physically consistent basin-wide warming anomaly over the whole SO, coexisting with a warm-polarity IPO-like pattern (EOF1 patterns for ERSST v4, v5, COBE, and COBE2; EOF2 for HadISST in Supplementary Fig. 2). The second mode shows a dipole pattern of opposite signs in the southeastern Pacific sector and other regions of the SO. The third mode is characterized by a zonally elongated zone stretching into a large swath of the SO. Because the last two modes diverge from one data to another (Supplementary Fig. 2), we use the EOF1 (EOF2 for HadISST) and its corresponding principal component to characterize the SOIDV pattern and temporal evolutions, respectively (Fig. 1a, b).

The SOIDV index features a quasi-40-year periodicity (Supplementary Fig. 4) with marked inter-decadal fluctuations roughly in phase with the IPO index (Fig. 1a). Significant simultaneous correlations exist between the SOIDV and IPO indices ( $R = 0.65$  for ERSST v4 and  $R > 0.7$  for other datasets at a 95% confidence level in Supplementary Fig. 5), indicating that the IPO accounts for about 40–50% (the square of correlation coefficients) of the SOIDV. However, no significant concurrent correlations appear between the SOIDV and AMV because the AMV impacts on the SO are entangled in the remaining modes (Supplementary Fig. 2). The stronger linkage of the SOIDV to IPO also manifests in the spatial homogeneity, especially the SO-wide same sign SST anomalies comparable to those in the tropical central-eastern Pacific (Fig. 1b). The correlation between the IPO and global SST further illustrates that a cold-phase IPO-SST anomaly generates a broad SO cooling (Fig. 1c), similar to the observed SO SST trend<sup>22,23</sup> for 1980–2013 (Fig. 1d).

To better understand the potential origin of recent SO cooling, we calculate the moving-window 34-year trends of SO SST linearly congruent

with the observed IPO trends using the linear regression coefficients of IPO against the global SST over 1900–2013 (termed IPO-congruent in Methods). The larger the observed IPO-index trends, the stronger the IPO-congruent trends of observed SO SST. Over the past century, the IPO-congruent trends in sign agree well with the observed (Supplementary Fig. 6a), albeit with reduced magnitudes in a few time windows. Particularly for three periods with maximum cooling of the SO SST during 1900–1933, 1977–2010, and 1980–2013 (Fig. 1e), and one period with maximum warming during 1953–1986 (Supplementary Fig. 6), an IPO-phase transition toward negative (positive) concurs with a SO cold (warm) episode. The broad agreement between the IPO-congruent and observed trends suggests the predominant influence of IPO on the SOIDV.

### Primary pathways for the IPO-SST anomaly triggering substantial SO climate change

We examine the physical pathways for conveying the IPO-SST signal to SO by restoring cold-polarity and warm-polarity IPO-SST patterns to observations in a state-of-the-art fully coupled climate model, IPSL-CM6A-LR (see Methods and Supplementary Fig. 7). We estimate the cold-phase IPO-induced SO climate response averaged over 10 years by subtracting an ensemble mean of the 10-member warm-phase IPO-SST restoring experiments from the cold-phase counterparts (denoted -IPO in Fig. 2). The cold-polarity IPO-SST restoring simulations produce a zonally asymmetric SST cooling over the SO (Fig. 2a), with strong cooling occupying the Pacific sector and moderate cooling across the Atlantic-Indian Ocean sectors, similar to the post-satellite observed trends<sup>19,30,31</sup>. However, a modest warm patch, not seen in observations (Fig. 1d and other SST datasets, including HadISST), appears in the Atlantic sector adjacent to the Antarctic Peninsula. This warming response may be initially triggered by the Ekman advection of warm waters southwards due to anomalous surface easterly winds and, after about 10 years, further maintained by the Ekman upwelling of warmer subsurface waters south of the Antarctic Circumpolar Current<sup>14,32</sup>.

The trans-hemispheric IPO-SO teleconnection is well-established via equivalent barotropic Rossby wave trains<sup>26,28</sup> (Fig. 2b, c), with alternating high-pressure and low-pressure anomalies that veer poleward and eastward, culminating in traversing the whole SO, as evidenced by the year-round wave activity<sup>33</sup> (Fig. 2b and Supplementary Fig. 8). Such anomalous circulation features facilitate a positive-polarity southern annular mode (SAM) tendency<sup>34,35</sup> (Fig. 2d), manifested as a dipole-like sea-level pressure pattern<sup>36</sup> with high-pressure centers near 40°S and low-pressure centers near 65°S, leading to a strengthening of the poleward-shifting westerlies across the SO (cf. Fig. 2a and Supplementary Fig. 7j).

Unlike typical La Niña episodes<sup>37,38</sup>, a cold-phase IPO-SST anomaly features meridionally broader cooling concurrent with larger warming over the diagonal poleward-extended South Pacific Convergence Zone (SPCZ). In response to the tropical Pacific basin-wide cooling, a strong southwestward-displaced SPCZ rainfall<sup>39,40</sup> (Fig. 3a), enhanced upper-level (200-hPa) convergence over the tropical western Pacific (Fig. 3b), and a reduced north-to-south cross-equatorial Hadley circulation subsequently ensue (Fig. 3c). Such conditions act in concert to sustain the year-round Rossby wave source situated south of the SPCZ<sup>41</sup> (Supplementary Fig. 9). As such, the cold-phase IPO-related SST cooling of tropical Pacific triggers the large-scale Rossby wave response that initially emanates over the subtropical western South Pacific and then propagates to the SO following a great arc. This Rossby wave train is characterized by anticyclonic anomalies east of New Zealand, cyclonic anomalies over the Amundsen Sea, and anticyclonic anomalies southeast of South America (Supplementary Fig. 8), reminiscent of the Pacific-South American-like pattern<sup>42</sup>.

Earlier studies indicate that the IPO and Pacific Decadal Oscillation (PDO) indices are highly correlated ( $R = \sim 0.9$ ,  $P < 0.05$ )<sup>43,44</sup>. Still, the IPO has a tropical Pacific origin, and the PDO has a more North Pacific focus<sup>43</sup>. These two distinct physical origins can communicate the tropical Pacific SST signal to SO through different physical pathways. To isolate the PDO-SO connection, we analyze the cold-phase and warm-phase PDO-SST restoring experiments (Methods). Compared to the cold-phase IPO, the

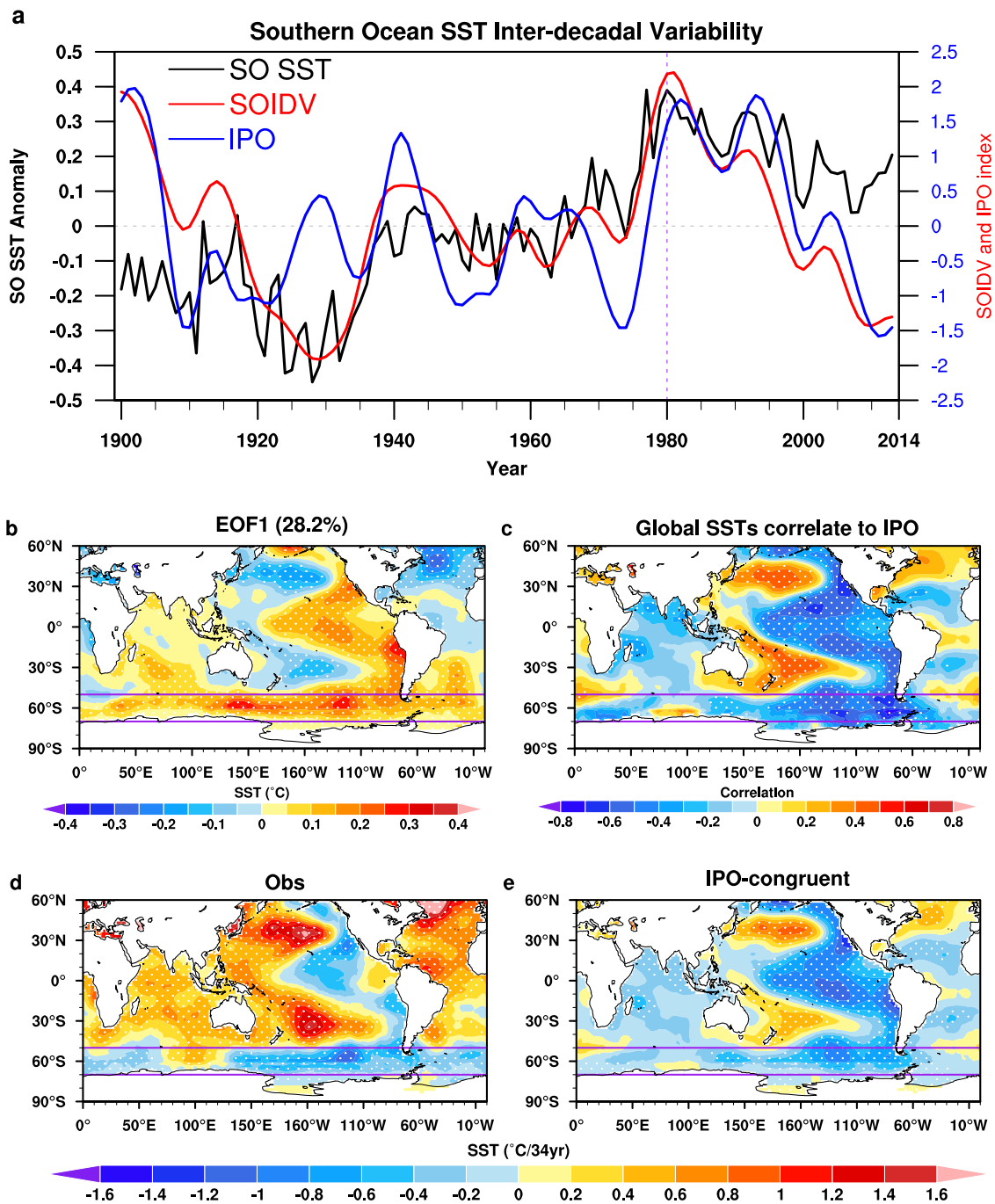


**Fig. 1 | The positive relationship between the inter-decadal Pacific Oscillation and the Southern Ocean inter-decadal variability.** **a** Time series of observed SO (50°S–70°S) annual-mean SST anomalies (black), the normalized Southern Ocean inter-decadal variability (SOIDV) index (red), and normalized inter-decadal Pacific Oscillation (IPO) index (blue) over 1900–2013. The observed SO SST anomalies are referenced to the climatology of 1900–2013. **b** The first principal pattern, representing the SOIDV spatial pattern, is obtained by applying an EOF to the quadratically detrended, 10-year low-pass-filtered annual-mean SST anomalies over the SO domain, explaining 28.2% of the total variance (ERSST v4). Beyond the SO domain, the associated pattern is obtained by regressing SST anomalies onto the first principal component (representing the SOIDV in **a**). **c** the synchronous correlation

coefficients with the IPO index. The global SST has been quadratically detrended and 10-year low-pass filtered. All correlation coefficients are multiplied by  $-1$  to facilitate the comparison with recent observed SST trends. **d** Observed SST trends during 1980–2013. **e** The 1980–2013 observed SST trends linearly congruent with the IPO-index trend (IPO-congruent). The IPO-congruent trends are computed by multiplying the regression coefficients for the IPO at each grid point in the linear regression of annual-mean SST anomalies against the IPO during 1900–2013 by the observed IPO-index trend over 1980–2013 (see Methods). Stippling indicates regions above the 95% significant level based on a Student’s two-sided  $t$ -test (**b, c**) and the Mann–Kendall test (**d, e**). The purple lines demarcate the SO domain (50°S–70°S). The observed SST dataset is based on ERSST V4.

negative-phase PDO-SST restoring reproduces weaker cooling across the SO (Fig. 2e), except for some patches of minor warming over the Pacific and Atlantic sectors. The modest SO cooling is linked to a diminished Rossby wave response (Fig. 2f, g), with anticyclonic anomalies east of New Zealand,

cyclonic anomalies over the Ross Sea, and anticyclonic anomalies southwest of South America before crossing the SO (Supplementary Fig. 8). Consistently, a positive-phase SAM anomaly of comparatively minor magnitude causes weak westerlies in the SO (0.28 in Fig. 2d and 0.25 in Fig. 2h for the

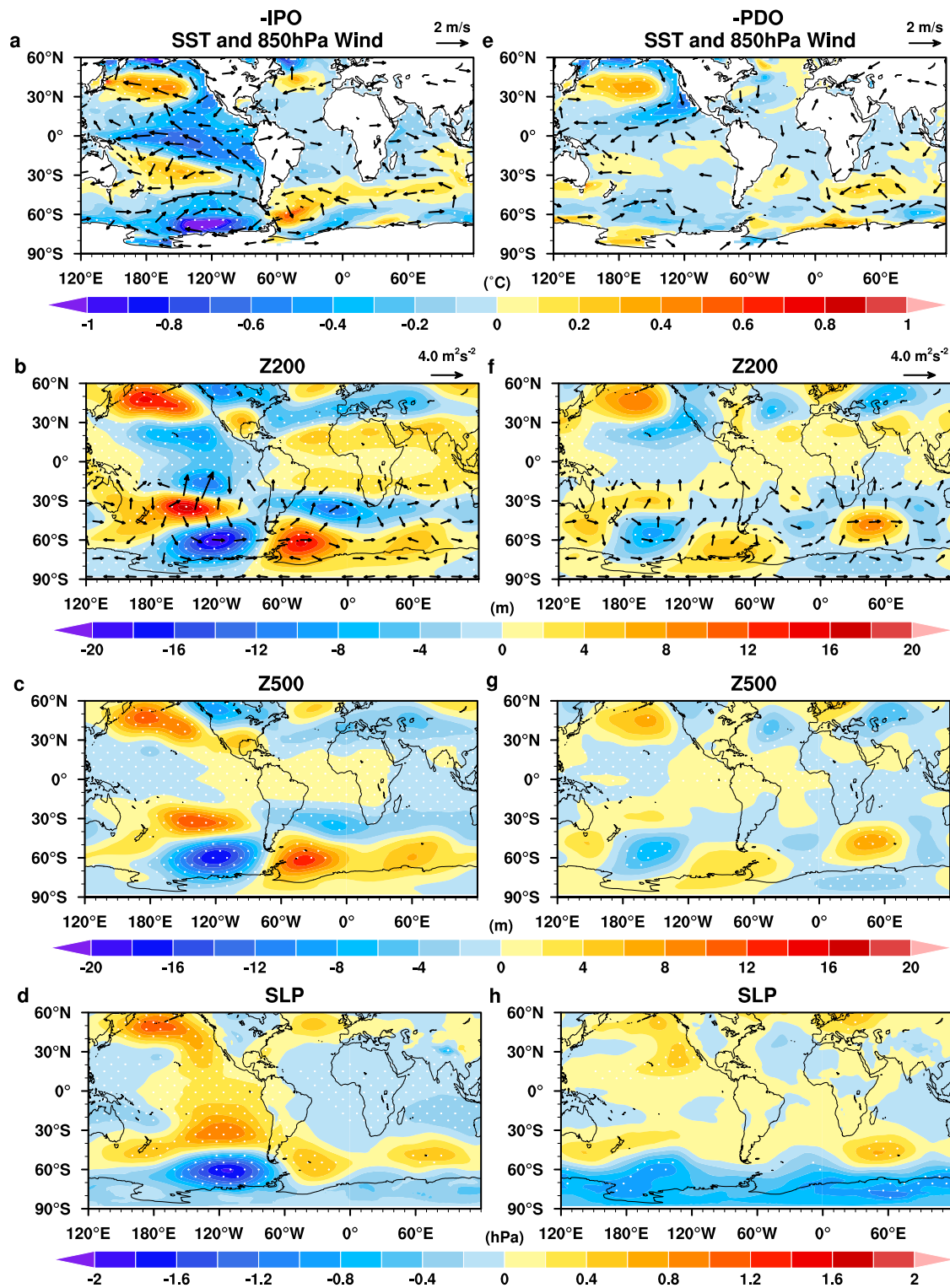


**Fig. 2 | Physical pathways for a cold-polarity IPO-SST to force the SO basin-wide SST changes.** **a** The SST (shading) and 850-hPa winds (vectors) responses to a warm-to-cold-phase switch of IPO in idealized restoring simulations. These responses are estimated by differencing annual-mean SST (850-hPa wind) changes averaged over ten years in the warm-phase IPO-SST runs from that in the counterpart cold-phase runs. **b** Same as in (a), but for 200-hPa geopotential height (Z200; shading) and wave activity flux (vectors) responses. **c** Same as in (a), but for 500-hPa geopotential height (Z500) response. **d** Same as in (a), but for sea-level pressure

(SLP). **e–h** Same as in **a–d**, but for responses to a warm-to-cold-phase transition of PDO. Note that the zonal mean of Z200 (Z500) at each latitude in **b**, **c** and **f**, **g** has been removed to illustrate the propagation of Rossby wave trains. The magnitude of the southern annular mode (SAM) index is estimated as the difference in the normalized zonally averaged SLP anomalies between 40°S and 65°S (0.28 for -IPO and 0.25 for -PDO). Stippling and vectors are only shown over regions where the changes are statistically significant above the 95% confidence level based on a Student's two-sided *t*-test.

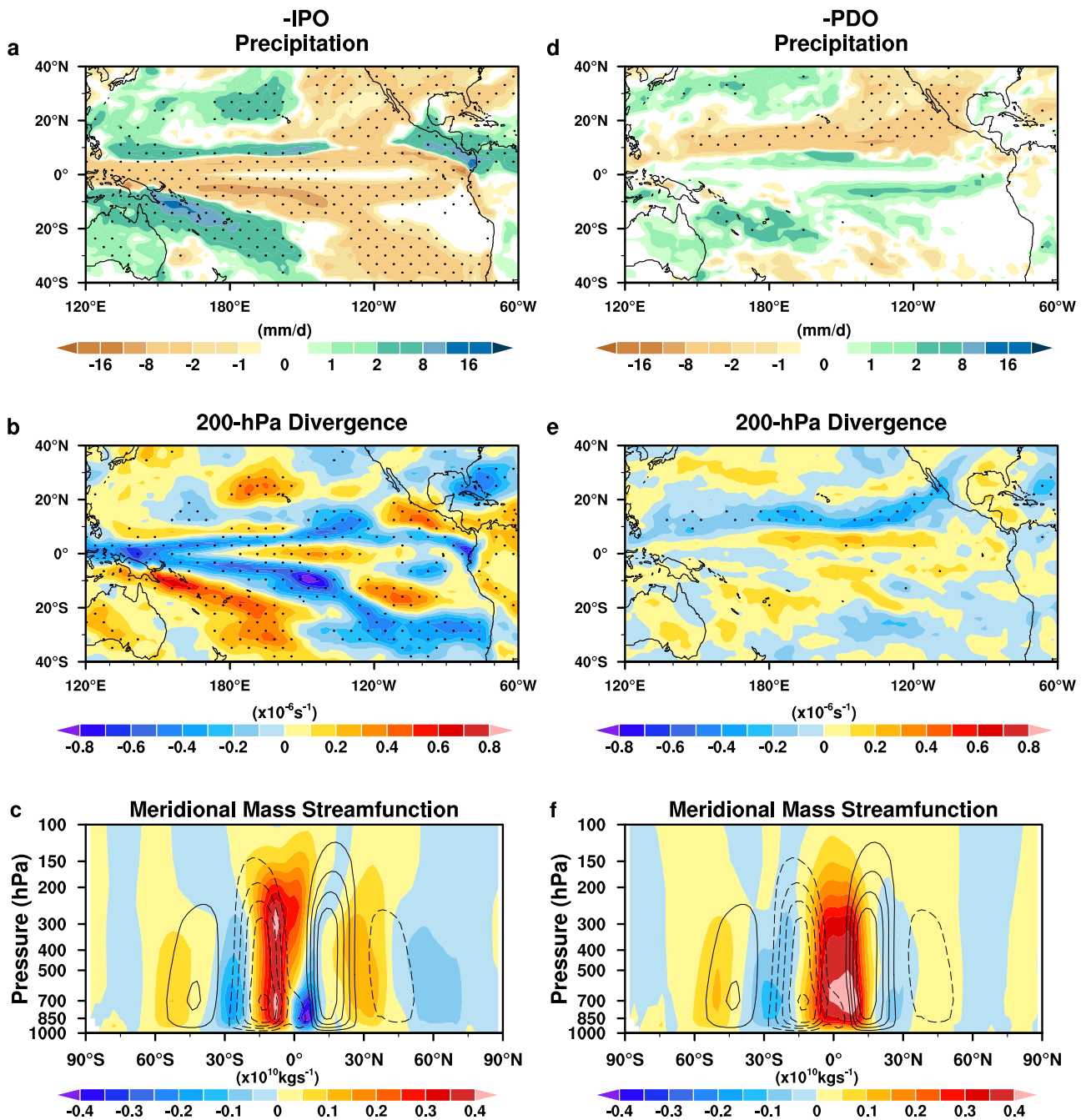


**Fig. 3 | The cold-polarity IPO-SST teleconnection to Southern Hemisphere atmospheric circulation.** **a** Precipitation response (shading in units of mm/d) to a warm-to-cold-phase shift of IPO in idealized restoring simulations. The response is estimated by subtracting annual-mean precipitation changes averaged over ten years in the warm-phase IPO-SST experiments from that in the counterpart cold-phase experiments. **b** Same as in (a), but for 200-hPa divergence response (shading in units of  $10^{-6} \text{ s}^{-1}$ ). **c** Same as in a, but for meridional mass streamfunction response

(shading in units of  $10^{10} \text{ kg s}^{-1}$ ), superimposed on the climatological distributions (dashed lines for negative values and solid lines for positive values) with an interval of  $0.2 \times 10^{11} \text{ kg s}^{-1}$  from  $-1.0 \times 10^{11} \text{ kg s}^{-1}$  to  $1.0 \times 10^{11} \text{ kg s}^{-1}$ . Positive values indicate clockwise flows and vice versa. **d–f** Same as in **a–c**, but for responses to a warm-to-cold-polarity transition of PDO. Stippling denotes regions where the changes are statistically significant above the 95% confidence level based on a Student's two-sided *t*-test.

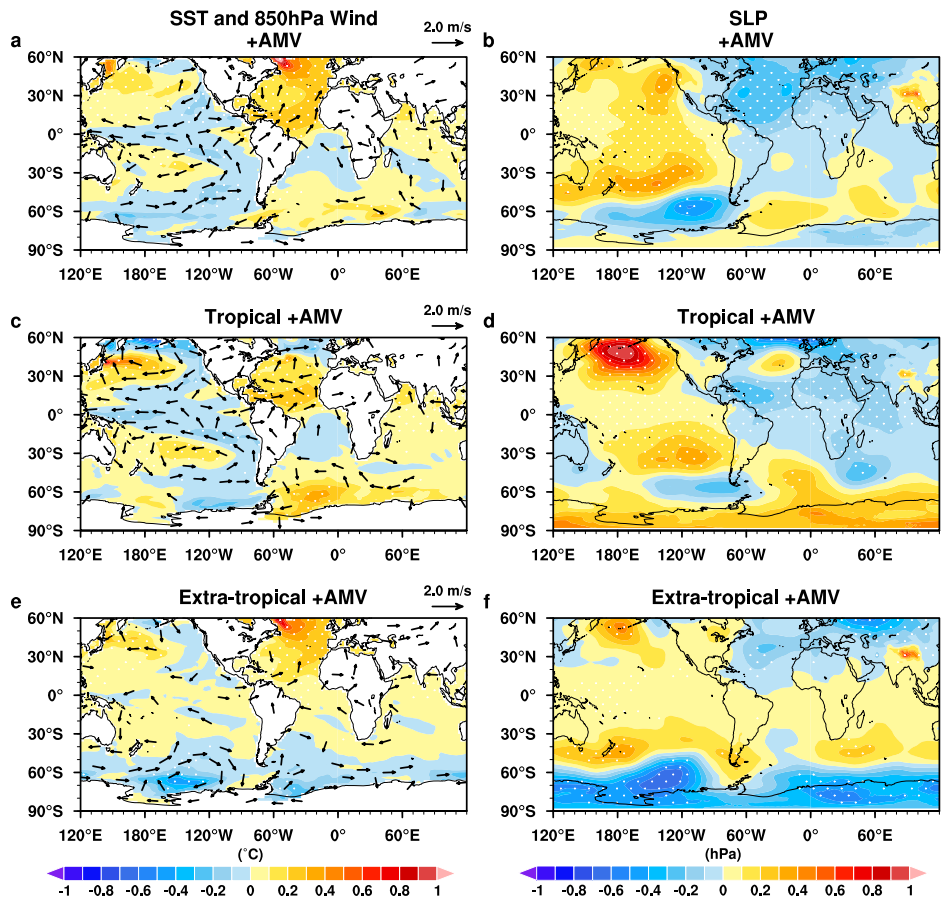
SAM index strength). This anomalous Rossby wave train activity largely corresponds to reduced cooling across the tropical Pacific (Fig. 2e), followed by slight northeastward extension of the weak SPCZ rainfall (Fig. 3d), attenuated upper-level convergence in the equatorial western Pacific (Fig. 3e), and diminished southward migration of the Hadley circulations (Fig. 3f). These unfavorable conditions collectively induce a modest Rossby wave source located south of SPCZ (Supplementary Fig. 9), thereby resulting in persistent Rossby wave trains of smaller magnitude compared to the cold-polarity IPO-SST-driven response. The sharp contrast between the

trans-hemispheric IPO-SO and PDO-SO teleconnections suggests that the tropical Pacific is an essential hotspot for transmitting the IPO-SST signature to the SO.

**Secondary pathways for the AMV-SST anomaly inducing moderate SO climate change**

Previous studies corroborate that a warm-phase AMV-SST forcing favors a cold-phase IPO-like SST anomaly through a strengthened Walker circulation<sup>45–47</sup>, implying an indirect influence on the SO from the

**Fig. 4 | Dynamical pathways for a warm-phase AMV-SST to affect the SO large-scale SST changes. a** The SST (shading) and 850-hPa winds (vectors) responses to a cold-to-warm-phase shift of AMV in idealized restoring simulations. These responses are calculated by subtracting annual-mean SST (850-hPa wind) changes averaged over 10 years in the cold-polarity AMV-SST experiments from that in the counterpart warm-polarity experiments. **b** Same as in **a**, but for sea-level pressure response (shading; SLP). **c, d** Same as in **a, b**, but for responses to a cold-to-warm-phase shift of tropical AMV-SST pattern. **e, f** Same as in **a, b**, but for responses to a cold-to-warm-polarity transition of extratropical AMV-SST pattern. Stippling and vectors are only shown over regions where the changes are statistically significant above the 95% confidence level based on a Student's two-sided *t*-test.



AMV-SST warming-forced tropical Pacific cooling similar in style to the IPO-SST-induced dynamical pathway (recall Fig. 2), in addition to a direct atmospheric response to the AMV-SST forcing<sup>24,48</sup>. We disentangle the two-pronged AMV teleconnections to the Southern Hemisphere extratropical atmosphere in the warm-phase and cold-phase AMV-SST restoring framework (Methods), wherein the AMV-SST pattern is further split into the tropical and extratropical domains to clarify their respective importance.

For a full AMV warm-polarity case, a prominent feature is that a negative-phase IPO-like SST response and a zonal cooling strip over the SO extending from the Indian Ocean sector to the Amundsen-Bellinghousen Seas emerge together (Fig. 4a), coinciding with the cyclonic wind pattern and associated low-pressure anomalies spanning from the Ross Sea to the Bellinghousen.

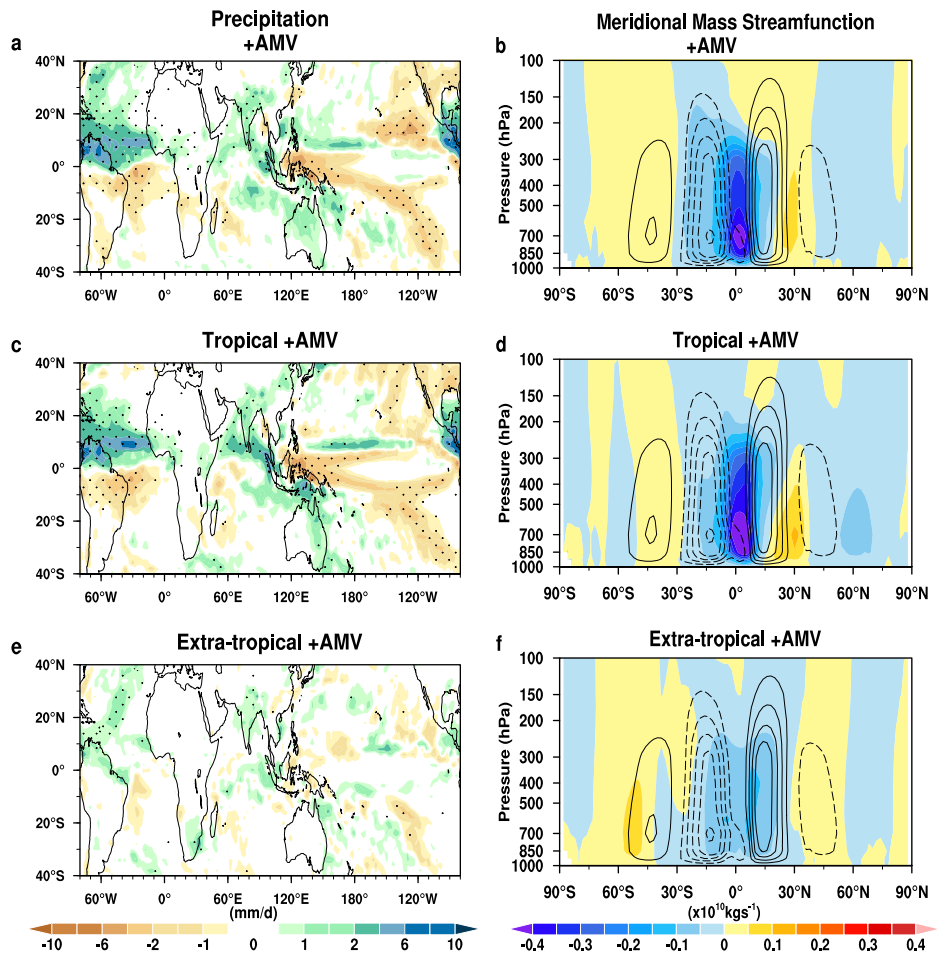
Sea (Fig. 4b). When forced by a tropical-only AMV-SST warming, SO SST cooling and cyclonic circulation anomalies are largely confined to the vicinity of the Amundsen Sea (Fig. 4c, d), despite broader cooling in the tropical Pacific. These AMV-SST warming-forced climatic changes are fairly distinct from ones by the IPO-SST cooling due to a southward extension of the weakened Hadley circulations (Fig. 3). Anomalous Atlantic warming, particularly in the tropical domain, triggers a strong northward displacement of the Atlantic inter-tropical convergence zone (ITCZ) (Fig. 5a, c). The corresponding upper-level (200-hPa) divergence fuels perturbations to a northward displacement of the intensified Hadley cells (Fig. 5b, d and Supplementary Fig. 10a, b), thus creating a stationary Rossby wave path from the subtropical South Atlantic to the Amundsen-Bellinghousen Seas (Supplementary Fig. 11). As a result, the trans-hemispheric AMV-SO teleconnections are likely a combination of two distinctive and contrasting Rossby wave trains. Specifically, an AMV-SST warming-induced Rossby wave response to a south-to-north cross-equatorial Hadley circulation intensification, partly negating the IPO-SST cooling-driven counterpart to a north-to-south cross-equatorial Hadley

cell weakening, contributes effectively to SST cooling across the Ross and Amundsen Seas.

By contrast, an extratropical-only AMV-SST forcing fails to capture the large tropical Pacific cooling, except for some patches of smaller cooling (Fig. 4e). Still, it forces a zonally elongated cooling band in the SO, albeit with a relatively weak magnitude than those generated by the cold-polarity IPO-SST and PDO-SST forcing (cf. Figs. 2, 4e). The SO-wide weak cooling is in better agreement with a poleward-extended westerly strengthening (Fig. 4e) and a positive-phase SAM anomaly (Fig. 4f), with the Amundsen Sea Low being shifted westward to the Ross Sea relative to the full and tropical-only AMV-SST forcing (Fig. 4). While the northward-displaced Atlantic ITCZ and the ensuing upper-level divergence have smaller strength compared to those in the full and tropical-only AMV-SST simulations (Fig. 5 and Supplementary Fig. 10), northward migration of the accelerated Hadley cells forms a westward-shifted planetary wave pathway, which is initially activated in the subtropical south Atlantic, and then steers eastward into the SO and ends in the Ross Sea (Supplementary Fig. 11). It is noteworthy that the sum of extratropical atmospheric responses to the extratropical-only and tropical-only AMV-SST forcing is not identical to the responses to the full AMV-SST forcing (cf. Fig. 4c, e, a), possibly owing to nonlinear processes or the model dependency<sup>46,47</sup>.

The distinct SO climatic responses to the cold-phase IPO-SST and warm-phase AMV-SST forcing in idealized restoring experiments provide sufficient evidence that the IPO is of first-order importance in modulating the SO SST inter-decadal variability, with the AMV being of subsidiary role. Although the cold-phase PDO and the extratropical-only AMV warm-polarity SSTs, to a lesser extent, act to cool the SO SST, they tend to provide an additional source of the SO inter-decadal variability in the absence of significant tropical Pacific cooling. The remainder of the study sheds light on the specific physical processes underpinning a cold IPO-SST phase to trigger basin-scale cooling in the SO.

**Fig. 5 | The warm-polarity AMV-SST teleconnections to Southern Hemisphere atmospheric circulation.** **a** Precipitation response (shading) to a cold-to-warm-polarity shift of AMV in idealized restoring simulations with IPSL-CM6A-LR. The response is estimated by subtracting annual-mean precipitation changes averaged over 10 years in the cold-phase AMV-SST experiments from that in the counterpart warm-phase experiments. **b** Same as in (a), but for meridional mass stream function response (shading in units of  $10^{10} \text{ kg s}^{-1}$ ), superimposed on the climatological distributions (dashed lines for negative values and solid lines for positive values) with an interval of  $0.2 \times 10^{11} \text{ kg s}^{-1}$  from  $-1.0 \times 10^{11} \text{ kg s}^{-1}$  to  $1.0 \times 10^{11} \text{ kg s}^{-1}$ . Positive values indicate clockwise flows and vice versa. **c, d** Same as in (a, b), but for responses to a cold-to-warm-polarity transition of tropical AMV-SST pattern. **e, f** Same as in (a, b), but for responses to a cold-to-warm-polarity transition of extratropical AMV-SST pattern. The hemispheric Hadley Circulation intensity is generally defined as the maximum value of the meridional mass stream function in the tropical zone. The Hadley Circulation strength index is calculated as the difference between the North (0–30°N) and South (0–30°S) Hemisphere Hadley Circulation strength indices. Thus, the Hadley Circulation strengths in **b, d, and f** are  $0.059 \times 10^{10} \text{ kg s}^{-1}$ ,  $0.089 \times 10^{10} \text{ kg s}^{-1}$ , and  $0.009 \times 10^{10} \text{ kg s}^{-1}$ , indicating a strengthened Hadley circulation response to a full warm-phase AMV-SST forcing (b), a tropical-only AMV warm-polarity SST forcing (d), and an extratropical-only AMV warm-polarity SST forcing (f), respectively. Stippling denotes regions where the changes are statistically significant above the 95% confidence level based on a Student's two-sided *t*-test.



**Key physical processes for a cold-phase IPO-SST governing SO basin-scale cooling**

To single out the potential causes of SO SST cooling, we decompose the cold-phase IPO-driven SO SST variability into dynamic (ocean dynamic processes) and thermodynamic (surface heat fluxes) components based on the ocean mixed-layer heat budget analysis<sup>49</sup> (Methods). Forced by the cold IPO-SST phase, a positive-phase SAM tendency translates into anomalous Ekman advection (Figs. 2, 6a). The resultant poleward-shifted westerly acceleration advects more cold waters northwards (Fig. 6b), leading to extensive cooling across a large swath of the Pacific sector (50°S–65°S) and the Atlantic and Indian Ocean sectors (55°S–70°S). Conversely, the easterly anomalies enhance the poleward Ekman transport of warmer waters, forming a narrow corridor of significant warming that spreads from the Ross Sea (65°S–70°S) into the South Atlantic sector (50°S–60°S), crossing the Drake Passage (Fig. 6b). Although the cold-polarity IPO-induced zonal-mean SST of SO exhibits a poleward-swelling cooling (Fig. 6c), the zonal-mean westerly peaks around 55°S (Fig. 6d), with remarkable physical consistency to the zonal-mean Ekman advection and equatorward Ekman transport of colder waters (Fig. 6e). It is important to note that the meridional SST gradients are relatively small in regions with climatological sea-ice cover. The weak meridional Ekman transport exerts little influence on SST changes. This discrepancy between the zonal distributions of SO SST and northward Ekman transport of cold waters indicates that other factors are required to explain sufficiently the poleward-growing SO cooling. However, both geostrophic advection and eddy diffusion are sporadic, and the vertical entrainment is negligible. Thus, they cannot adequately explain the large-scale SO cooling (Supplementary Fig. 12).

On the other hand, surface net shortwave radiation reduction closely matches the poleward-accumulative cooling across the Ross-Amundsen

Seas (Fig. 6f), primarily through the shortwave cloud-radiative effect because of the increased total cloud fraction (Fig. 6h and Supplementary Fig. 12f). A small diminution of surface net longwave radiation is conducive to yielding moderate cooling across parts of the Ross-Amundsen Seas and South Atlantic-Indian Ocean sectors (Fig. 6g) due to the reduced cloud cover (Supplementary Fig. 12f). However, the increased cloud cover over much of the Pacific sector may cause warm SST anomalies via longwave cloud-radiative effect (Fig. 6i), partially compensating for cold SST anomalies induced by shortwave cloud-radiative effect. Eventually, the shortwave cloud-radiative effect dominates the poleward-growing cooling in the Pacific domain of the high-latitude SO (cf. Fig. 6h, i). Decreases in the latent and sensible heat flux also generate cooling patches in the SO (Supplementary Fig. 12), albeit with comparatively weaker magnitude than the shortwave cloud-radiative effect. Taken together, the diagnosis of SO surface heat balance offers confidence that the enhanced northward Ekman transport of cold waters and shortwave cloud-radiation effect should be collectively responsible for the SO basin-wide cooling response to a cold-polarity IPO-SST anomaly, given the complexity of SO SST inter-decadal variability.

**Discussion**

The proposed physical mechanisms underlying the decadal-timescale impact of the tropical Pacific on the SO are only based on the IPSL-CM6A-LR model. Whether the main results operate in other model configurations, such as CNRM-CM6-1 (ref. 50), has yet to be determined. In the two global climate models, the identical restoring framework is adopted to perform idealized experiments forced with the IPO-SST and AMV-SST anomalies as part of the Decadal Climate Prediction Project<sup>51</sup> of CMIP6. In response to a cold-phase IPO-SST anomaly, both models show a similar broad cooling

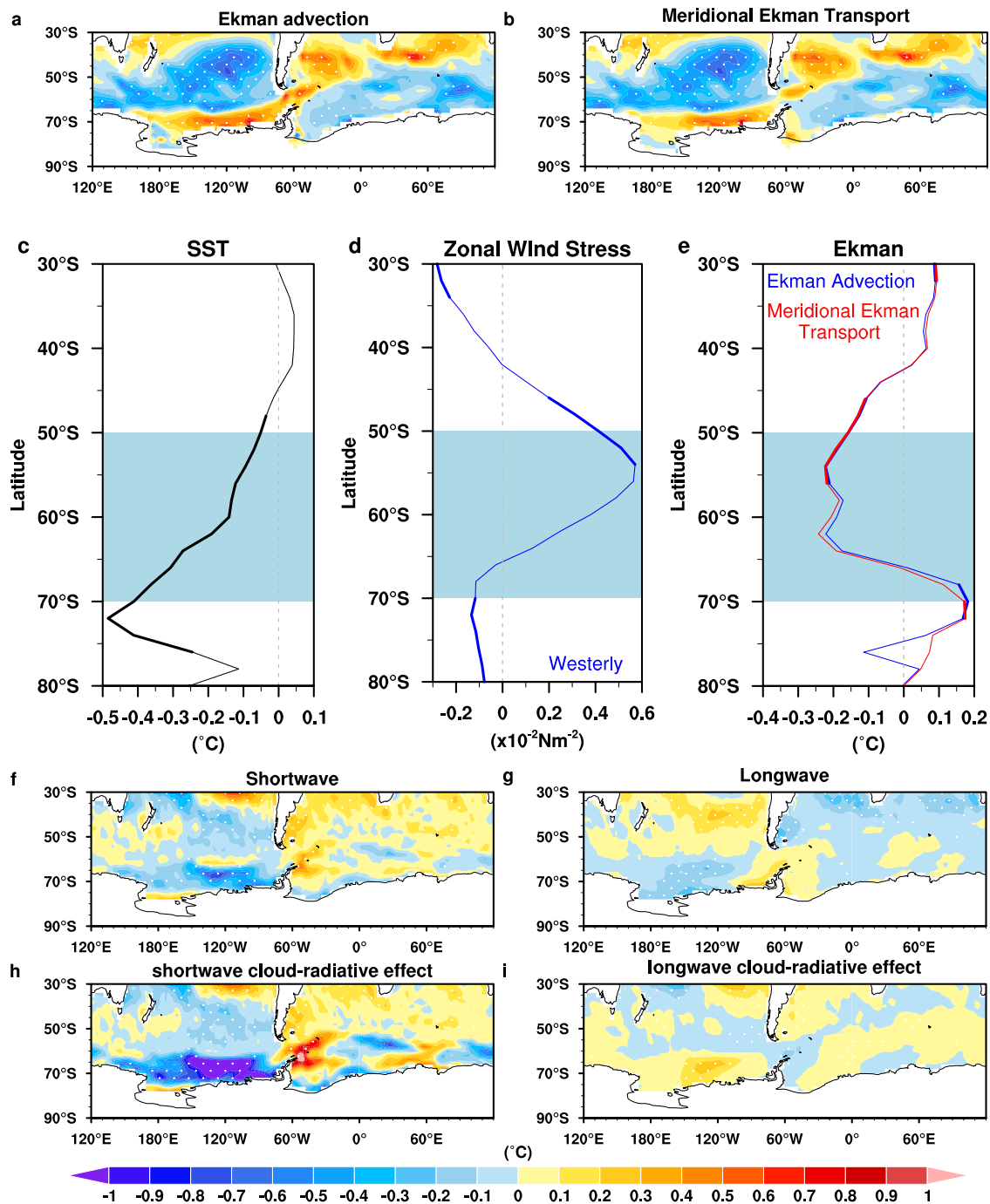


**Fig. 6 | Physical processes involved in the SO SST variability driven by a cold-polarity IPO-SST anomaly.** **a** The Ekman advection response (shading) to a warm-to-cold-polarity shift of IPO in idealized restoring simulations. The responses are computed by subtracting annual-mean Ekman advection changes averaged over ten years in the warm-phase IPO-SST experiments from its cold-phase counterparts. **b** Same as in (a), but for the meridional Ekman transport. Negative (Positive) values in **a** and **b** denote the northward (southward) Ekman transport of cold (warm) waters, cooling (heating) the SO SST. **c** The zonal average of SST response (black thin line). **d** The zonal mean of zonal wind stress (blue thin line). **e** The zonal mean of Ekman advection (blue thin line) and meridional Ekman transport (red thin line).

**f** Same as in (a), but for net surface shortwave radiation. **g** Same as in (a), but for net surface longwave radiation. **h** Same as in (a), but for shortwave cloud-radiative effect. **i** Same as in (a), but for longwave cloud-radiative effect. The cloud-radiative effect is calculated by taking the difference between all-sky and clear-sky net irradiance flux at the top of the atmosphere. Positive radiation flux denotes that the ocean absorbs heat from the atmosphere, heating the SO SST. In contrast, negative radiation flux indicates that the ocean loses heat to the atmosphere, cooling the SO. The stippling area and thick lines are statistically significant above the 95% confidence level based on a Student's two-sided *t*-test.

pattern and circumglobal teleconnection structure of distinct wavenumber-3 shape over the SO (cf. Fig. 2 and Supplementary Fig. S13). Although a cold-polarity PDO-SST anomaly also drives a relatively weak SO large-scale cooling and a circum-SO teleconnection pattern in both models, the anomalous Amundsen Sea Low is considerably shifted eastward by

~40°–50° longitudes in CNRM-CM6-1 relative to IPSL-CM6A-LR (cf. Fig. 2 and Supplementary Fig. S13). Notably, in the IPO-SST and PDO-SST simulations, the CNRM-CM6-1 cannot successfully reproduce a positive-phase SAM anomaly due to the model deficiencies and atmospheric internal variability in the Southern Hemisphere compared to the IPSL-CM6A-LR.



Moreover, a warm-polarity AMV-SST anomaly in CNRM-CM6-1, particularly in the extratropical part, creates significant cooling concentrated in the Amundsen Sea (Supplementary Fig. S14), quite distinct from extensive cooling over the whole SO in IPSL-CM6A-LR (cf. Fig. 4 and Supplementary Fig. S14). This disagreement in the two models suggests that the simulated SO SST response to an AMV-SST forcing is somewhat model-dependent. The quantitative comparison of the two models supports our conclusion that the tropical Pacific is decisive for modulating the SO basin-wide SST changes on the decadal timescales, with a small yet distinct contribution from the Atlantic. Thus, we argue that, due to the compensating effects of the IPO-SST and AMV-SST forcing, the out-of-phase relation between the IPO and AMV leads to strong SO SST inter-decadal variability. By contrast, the in-phase relationship between the IPO and AMV produces relatively weak SO SST inter-decadal variability. Since around 2015, the IPO phase has experienced a shift from cold-to warm, and the warm-polarity AMV has persisted since 1980. The in-phase effects of the IPO and AMV would likely weaken the SO SST inter-decadal variability in the forthcoming decades (e.g., 20–30 years).

The current global climate models may have underestimated the SO SST inter-decadal variability due to the unrealistic representation of inter-decadal to multidecadal SST variability associated with the IPO and AMV. For example, a cold-phase IPO-SST anomaly facilitates stronger cooling in the Pacific sector of SO in IPSL-CM6A-LR than in CNRM-CM6-1 (cf. Fig. 2a and Supplementary Fig. S13a). By comparison, a cold-polarity PDO-SST anomaly produces broader cooling in the tropical Pacific and, thus, more extensive cooling over the SO in CNRM-CM6-1 than in IPSL-CM6A-LR (cf. Fig. 2e and Supplementary Fig. S13e). Additionally, a warm-polarity AMV-SST anomaly, especially in the tropical domain, triggers a cold-polarity IPO-like pattern in IPSL-CM6A-LR (Fig. 4a, c), consistent with earlier findings<sup>45–47</sup>, which is missing in CNRM-CM6-1 (Supplementary Fig. S14a, c). A warm-phase extratropical-only AMV-SST anomaly forces significant cooling across the SO in IPSL-CM6A-LR (Fig. 4e), but a significant cooling belt is only confined to the Amundsen Sea in CNRM-CM6-1 (Supplementary Fig. S14e). While these potential biases persist in current climate models participating in the Decadal Climate Prediction Project<sup>51</sup> as part of CMIP6, the multi-model idealized restoring experiments with the IPO-SST and AMV-SST anomalies provide great impetus to improve our understanding of the trans-hemispheric tropical-SO connections on decadal timescales.

We have revealed a strong positive relationship between the IPO and the SO SST inter-decadal variability in observations. When a simulated IPO phase shifts from positive toward negative, a basin-wide SO cooling arises mostly from a strong Rossby wave response to a southward-displaced Hadley cell weakening forced by tropical Pacific broad cooling. The converse occurs for a cold-to-warm-phase transition of IPO. In a distinct style to the IPO, a warm-polarity AMV-SST anomaly, especially spawned in the extratropical part, contributes partly to SO SST large-scale cooling through a weaker Rossby wave response to a northward-shifted Hadley circulation intensification. Our results suggest that the tropical Pacific is a fundamental determinant for establishing the tropical-SO teleconnections on decadal timescales, with the Atlantic playing a smaller role. Furthermore, in a negative-polarity IPO case, the enhanced northward Ekman transport of colder waters associated with the poleward westerly strengthening acts in tandem with the shortwave cloud-radiative effect to make the SO SST basin-wide cooling persist for a period (i.e., ~10 years).

While the IPO explains ~40–50% of the SO SST inter-decadal variability through a fast mixed-layer response (~10 years) to the tropical Pacific-SO teleconnection, the other driver, such as the deep convection of multidecadal climate variability intrinsic to the SO associated with the Antarctic Bottom Water (AABW) formation<sup>7,23</sup>, may play an indispensable part through a slow adjustment process (~30 years or even longer). For example, the SO SST experienced substantial cooling over the post-satellite period of 1980–2013 (Fig. 1d), concurring with a negative-phase IPO-SST pattern. In addition to a transient response to the tropical Pacific cooling, the long-lasting cooling in the SO may be further sustained by the halted deep

convection due to a spin-down of the AABW<sup>7,23</sup>. Further, our findings of the tropical Pacific-to-SO decadal teleconnection and recent results of the SO-to-southeastern tropical Pacific teleconnection<sup>52,53</sup> suggest the sequential two-way interactions between the tropical Pacific and the SO, both widely underrepresented in current climate models. Thus, an in-depth understanding of SO SST inter-decadal variability could be imperative to constrain near-term predictions and future projections of tropical Pacific climate, which, in turn, provides the potential to improve model estimates of climate sensitivity<sup>54</sup> and climate feedback.

## Methods

### Observational and CMIP6 datasets

Five different SST products, including ERSST v4, v5 (Extended Reconstructed Sea Surface Temperature version 4 and 5)<sup>55,56</sup>, COBE-SST and COBE-SST2 (Centennial in situ Observation-Based Estimates of Sea Surface Temperature)<sup>57</sup>, and HadISST (Hadley Center Sea Ice and SST dataset)<sup>58</sup> spanning from 1891 to 2019, were employed to characterize the pronounced inter-decadal fluctuations in the observed Southern Ocean (SO; 50°S–70°S) SST (Supplementary Fig. 1). Because the observed SSTs are more reliable over the common period 1900–2013, annual anomalies of observed SSTs were constructed relative to annual-mean climatology of 1900–2013 in each dataset and then quadratically detrended to remove the influence of greenhouse-induced warming. The observed SO SST before the satellite-era may not be high-quality<sup>6,59</sup>. However, establishing whether recent SO cooling is unusual and whether the SO inter-decadal variability is robust requires more past climate information that extends beyond the satellite-era period.

We applied an Empirical Orthogonal Function (EOF) decomposition into the 10-year low-pass-filtered (Butterworth filter) SO SSTs in each dataset to extract the observed SO inter-decadal variability. The leading EOFs (EOF1; EOF2 for HadISST), representing the SO SST inter-decadal variability pattern (Supplementary Fig. 2), explain ~21.8–33.9% of the decade-to-decade variance and are distinctly separated from the remaining eigenvectors (e.g., EOF2 and EOF3) based on the North et al. criterion (ref. 60). The principal component (PC1; PC2 for HadISST) associated with EOF1 (EOF2 for HadISST) is defined as the SO inter-decadal variability (SOIDV) index (Fig. 1 and Supplementary Fig. 3). The EOF2 and EOF3 patterns differ from one data to another, implying that uncertainties and potential errors exist among different SST datasets.

Given the discrepancy between HadISST and other SSTs (Supplementary Figs. 2–5), we should be cautious in interpreting the observed characteristics of SO inter-decadal variability. We emphasize that this study is intended to quantify the relative importance of the IPO and AMV in mediating the SO inter-decadal variability and further shed light on the underlying physical mechanisms but rather to give a quantitative evaluation of observed SO inter-decadal variability. Unless otherwise stated, the observed and simulated results in the main text are based on ERSST v4 because of its more common usage in the Decadal Climate Prediction Project designed for the CMIP6.

We also take model outputs from the sixth Coupled Model Inter-comparison Project (CMIP6) historical runs to demonstrate that the external forcing fails to reproduce the pronounced inter-decadal variability observed in the SO SST (Supplementary Fig. 1).

### Analyses methods and significance testing

The Theil-Sen method<sup>61</sup> was utilized to compute the observed SST trends with 95% confidence intervals based on the Mann-Kendall test (Fig. 1 and Supplementary Fig. 6). We measured the statistical significance of the correlation and linear regression coefficients according to a Student's two-sided *t*-test in which the effective number of degrees of freedom was estimated using the lag-1 autocorrelation of the two series<sup>62</sup>. We also employed the Student's *t*-test to examine the confidence interval of the simulated SO climate responses to the IPO-SST and AMV-SST anomalies in idealized restoring experiments described below.

## IPO and AMV indices and their corresponding spatial patterns

Following the previously proposed methods<sup>46,47,63</sup>, we estimated the internally generated components of observed Inter-decadal Pacific Oscillation (IPO) and Atlantic Multidecadal Variability (AMV). By conducting a signal-to-noise maximizing EOF decomposition into global annual-mean SST from the CMIP5 multi-model historical experiments covering 1890–2005 and representation concentration pathway 8.5 (RCP8.5) until 2020, we extracted the first principal component (PC1) associated to the leading global signal-to-noise EOF SST. The spatial pattern associated with the externally forced component of SST was taken by regressing the observed global annual-mean SST against PC1.

After subtracting the CMIP5-based radiatively-forced component from the observed annual-mean SST, we performed an EOF analysis of the residual SST over the Pacific-wide domain (40°S–70°N, from Indonesia to the American coast). The first principal component was extracted and filtered via a zero-phasing Butterworth filter to reflect the temporal evolution of the IPO index. Correspondingly, regression of the residual SST at each grid point upon the IPO index over 1900–2013 represents the IPO-SST spatial pattern (Supplementary Fig. 7). Similarly to the IPO, the weighted average of the residual annual-mean SST over the North Atlantic domain (0°–60°N, from the American coast to Africa/Europe) is defined as the AMV index after filtering using a zero-phasing Butterworth filter. We obtain the AMV-SST spatial patterns by regressing the residual annual-mean SST at each grid point onto the AMV index over 1900–2013 (Supplementary Fig. 7). Notably, introducing the same zero-phasing Butterworth filter to the SOIDV, IPO, and AMV indices in each data enables us to make an objective assessment of their lead-lag statistical relationships (Supplementary Fig. 5). The IPO-SST and AMV-SST spatial patterns (ERSST v4) are prescribed in idealized restoring experiments described below to examine their respective importance to the SOIDV.

## Observed SO SST changes linearly congruent to the observed IPO trends

Given the irregularity of IPO in terms of magnitude and phase transition<sup>22,64</sup>, we examine the role of the IPO phase shift in generating the observed SO SST changes by quantifying how much observed SO SST trends are linearly congruent with the observed IPO trends (hereafter called IPO-congruent trends). For example, during 1980–2013, the IPO phase shifted toward warm from cold, and the SO SST underwent extensive cooling (Fig. 1). We first regress the observed annual-mean global SST (ERSST v4) at each grid point onto the observed IPO index over 1900–2013. The consequent regression coefficients over the SO are then multiplied by rolling-window 34-year trends of the observed IPO index ranging from 1900–1933 to 1980–2013 (Fig. 1 and Supplementary Fig. 6).

## Idealized restoring experiments

To disentangle the physical pathways communicating the IPO-SST and AMV-SST signals to the SO, we analyze five suites of IPO-SST and AMV-SST-nudging experiments conducted with a fully coupled climate model, termed IPSL-CM6A-LR<sup>65</sup>, as a contribution to the CMIP6 Decadal Climate Prediction Project<sup>51</sup>. The IPSL-CM6A-LR has an equilibrium climate sensitivity (ECS: 4.7 °C) and transient climate response (TCR: 2.35 °C) close to the mean ECS and TCR estimated by previous studies<sup>66</sup>. We evaluate the present-day climatology of SST and precipitation in IPSL-CM6A-LR against observations by considering the common period of 1980–2013 (Supplementary Fig. 7). Although the IPSL-CM6A-LR is greatly improved compared to previous versions, the common biases and shortcomings, including an excessively westward-extended cold tongue, double Inter-tropical Convergence zone, etc., persist. However, as shown in previous studies<sup>47,67</sup> of the detailed model configurations, the IPSL-CM6A-LR idealized restoring simulations have successfully captured the tropical Pacific-Atlantic inter-basin climate interactions on decadal timescales.

In the first two experiments, SSTs over the whole Pacific (40°S–70°N) and North Pacific (20°N–70°N) are nudged, respectively, towards both negative-polarity and positive-polarity patterns of IPO and PDO

superimposed on the climatologically-varying model control-run SST (Supplementary Fig. 7). Although the IPO and PDO indices are significantly correlated ( $R = -0.9$ ,  $P > 0.05$ )<sup>44</sup>, they have distinctive physical origins<sup>43</sup>. Specifically, the IPO primarily reflects the tropical Pacific processes, with high coherence over the North and South Pacific<sup>68</sup>. Instead, although the PDO represents a combination of remote tropical forcing and local North Pacific variability, it has more of a North Pacific focus. Accordingly, the IPO-SST and PDO-SST restoring experiments could help us distinguish their relative importance to the SO SST inter-decadal variability.

In the remaining three experiments, SSTs over the full North Atlantic (0°–60°N), tropical North Atlantic (0°–30°N), and extratropical Atlantic (30°N–60°N) are constrained, respectively, to both warm-phase and cold-phase patterns of full AMV, tropical-only AMV, and extratropical-only AMV overlaid on model control-run climatology (Supplementary Fig. 7). These distinct AMV-SST-nudging experiments aim to single out their respective role in forcing the SO SST variability.

The targeted SST patterns are kept constant in these SST-nudging simulations. Each experiment lasts ten years, and all radiative forcing agents are fixed at the pre-industrial levels. There are ten ensemble realizations for the IPO-SST and PDO-SST restoring simulations and 25 ensemble members for the AMV-SST restoring simulations. To maximize the signal-to-noise ratio and determine more reliably the influence of a warm-to-cold-phase transition of IPO or PDO (overlooking a neutral state), we estimate the simulated SO climate response to a cold-phase IPO-SST (PDO-SST) forcing by comparing the ensemble mean of 10-member cold-polarity IPO-SST (PDO-SST) runs averaged over 10 years to their warm-polarity counterparts (Figs. 2, 3). A similar procedure is performed for the AMV-SST restoring experiments to calculate their respective model responses (Figs. 4, 5). When separately taking ten ensemble members of IPO-SST (PDO-SST) and AMV-SST restoring experiments as the ensemble mean, our main conclusions hold that the SO SST inter-decadal variability mostly stems from the IPO, with a smaller contribution from the AMV, especially in the extratropical domain.

The five idealized restoring experiments with CNRM-CM6-1 participating in the Decadal Climate Prediction Project of CMIP6 are also presented to test whether the dominance of tropical Pacific over the trans-hemispheric tropical-SO teleconnections on decadal timescales derived from IPSL-CM6A-LR is model-dependent (Supplementary Figs. S13, S14). The comparison of idealized restoring simulation results from the two climate models adds model diversity to our diagnosis and confidence in the robustness of our main conclusion.

## Rossby wave activity flux

Using idealized restoring experiments described above, we diagnose wave activity flux<sup>33</sup> to detect large-scale quasi-stationary Rossby wave propagation in the Southern Hemisphere extratropical atmosphere. The wave flux vectors (Fig. 2), highly parallel to the group velocity of stationary Rossby waves, are useful for uncovering an eastward-propagating large-scale Rossby wave train initiated by a cold-phase IPO-SST or warm-polarity AMV-SST forcing.

## Rossby wave source

To validate the initiation and development of extratropical atmospheric Rossby waves in the Southern Hemisphere, we gauge the Rossby wave activity by diagnosing the 200-hPa barotropic vorticity equation following an earlier study<sup>69</sup>. The Rossby wave source (RWS) is well approximated as

$$RWS = -V_{\chi} \cdot \nabla(\xi + f) - (\xi + f)D \quad (1)$$

where  $V_{\chi}$  and  $D$  denote the divergent wind and divergence at 200 hPa, respectively;  $\xi$  is relative vorticity, and  $f$  the Coriolis parameter. The two right-hand terms in Eq. (1) represent the vorticity advection linked to the divergent wind and the vorticity generation by vortex stretching, respectively. Because of the high dependence on the divergent flow and nonzero absolute vorticity, RWS is comparatively weak over the equatorial

domain but is nonlocal and centralized in the subtropics, wherein the climatological westerly flow facilitates the generation of the Rossby wave.

### Atmospheric meridional mass stream function

We calculate the meridional mass stream function to reveal the IPO-SST and AMV-SST impacts on Southern Hemisphere atmospheric meridional circulation (Figs. 3, 5). The meridional mass stream function ( $\psi_m$ ) is estimated by vertically integrating the zonal-mean meridional wind from the top of the atmosphere to the surface, defined as follows:

$$\psi_m = \frac{2\pi\alpha \cos(\phi)}{g} \int_p^{p_s} v dp \quad (2)$$

Here  $v$  is zonal mean meridional winds;  $\alpha$  is Earth's radius (~6378 km);  $\phi$  is latitude (radians);  $g$  is the acceleration of gravity (9.8 ms<sup>-2</sup>);  $p$  is the pressure, and  $p_s$  denotes the surface pressure.

While cold-polarity IPO-induced and warm-phase AMV-induced Hadley circulation modifications are more regional, these local perturbations are sufficient to influence zonal-mean meridional stream functions (Figs. 3, 4).

### Mixed-layer heat budget analysis

The SO SST variability is controlled through the heat balance in the ocean mixed layer<sup>49</sup>, comprising surface net air-sea heat flux (the first four right-hand terms in the equation below), Ekman and Geostrophic horizontal advection (5th and 6th terms), and diffusive process (7th term) in the mixed-layer depth, and Entrainment process (8th term) at the bottom of the mixed layer.

$$\frac{\partial T}{\partial t} = \frac{1}{\rho_0 C_p h_m} (Q_{sw} + Q_{lw} + Q_{lh} + Q_{sh}) - \vec{V}_E \cdot \nabla T - \vec{V}_G \cdot \nabla T + \kappa_H \nabla^2 T + \frac{w_e (T_b - T)}{h_m} \quad (3)$$

where  $T$ ,  $T_b$ , and  $h_m$  are SST, the ocean potential temperature just below the mixed-layer depth, and the mixed-layer depth, respectively;  $\rho_0$  (1027 kg m<sup>-3</sup>) is the reference density of seawater;  $C_p$  (4000 J kg<sup>-1</sup> K<sup>-1</sup>) is the specific heat capacity of seawater at constant pressure;  $Q_{sw}$ ,  $Q_{lw}$ ,  $Q_{lh}$ , and  $Q_{sh}$  indicate surface net shortwave radiative flux, net longwave radiative flux, latent heat flux, and sensible heat flux, respectively;  $\vec{V}_E$  and  $\vec{V}_G$  are Ekman and Geostrophic current velocities, respectively;  $\kappa_H$  is the eddy diffusivity (here set to be 500 m<sup>2</sup> s<sup>-1</sup>);  $w_e$  denotes the entrainment rate and is estimated as the sum of the rate of change in the mixed layer depth and the Ekman vertical current velocity. The downward shortwave radiative flux at the base of the mixed-layer depth serves as a second-order factor compared to other terms in Eq. (3) and hence is ignored.

Here, we focus on the simulated SO heat balance derived from the cold-polarity IPO-SST restoring experiments. Specifically, a cold-phase IPO-SST anomaly leads to SO SST basin-scale cooling via the enhanced northward Ekman transport of colder waters associated with the accelerated westerly anomalies (Fig. 6 and Supplementary Fig. 12). Conversely, a warm-phase IPO-SST anomaly forces basin-scale warming in the SO. We also calculate the simulated SO heat balance in the cold-phase PDO-SST and warm-polarity AMV-SST restoring experiments. Compared to a cold-polarity IPO-SST forcing, the PDO-SST cooling and the AMV-SST warming, particularly in the extratropical part, are both minor in generating the SO SST large-scale cooling, primarily due to the comparatively weak poleward-shifted westerlies forced by the tropical Pacific small cooling and the Atlantic SST warming, respectively (not shown).

### Data availability

The observed SST datasets and model outputs that support this study are publicly available from the following websites: ERSST v4 and v5 (<https://www.ncei.noaa.gov/products/extended-reconstructed-sst>), COBE SST and

SST2 (<https://psl.noaa.gov/data/gridded/index.html>), and HadISST (<https://www.metoffice.gov.uk/hadobs/hadisst/>). All the CMIP6 model outputs are available at <https://pcmdi.llnl.gov/CMIP6>. More data about the idealized restoring experiments are provided upon reasonable request.

### Code availability

The codes used here to generate all the main figures are available upon request from the corresponding author, S.L.Y. The codes are created using the NCAR Command Language (NCL: <https://www.ncl.ucar.edu/>), a public access software.

Received: 4 November 2023; Accepted: 8 May 2024;

Published online: 16 May 2024

### References

- Eyring, V. et al. Human Influence on the Climate System. In *Climate Change 2021: The Physical Science Basis. Contribution of Working Group I to the Sixth Assessment Report of the Intergovernmental Panel on Climate Change* (eds. Masson-Delmotte, V. P. et al.) 423–552 (Cambridge University Press, Cambridge, 2021). <https://doi.org/10.1017/9781009157896.005>.
- Frölicher, T. L. et al. Dominance of the Southern Ocean in anthropogenic carbon and heat uptake in CMIP5 models. *J. Clim.* **28**, 862–886 (2015).
- Sallée, J.-B. Southern ocean warming. *Oceanography* **31**, 52–62 (2018).
- Sabine, C. L. et al. The oceanic sink for anthropogenic CO<sub>2</sub>. *Science* **305**, 367–371 (2004).
- Landschützer, P. et al. The reinvigoration of the Southern Ocean carbon sink. *Science* **349**, 1221–1224 (2015).
- Fan, T., Deser, C. & Schneider, D. P. Recent Antarctic sea ice trends in the context of Southern Ocean surface climate variations since 1950. *Geophys. Res. Lett.* **41**, 2419–2426 (2014).
- Latif, M., Martin, T. & Park, W. Southern Ocean sector centennial climate variability and recent decadal trends. *J. Clim.* **26**, 7767–7782 (2013).
- Cook, E., Buckley, B., D'arrigo, R. & Peterson, M. Warm-season temperatures since 1600 BC reconstructed from Tasmanian tree rings and their relationship to large-scale sea surface temperature anomalies. *Clim. Dyn.* **16**, 79–91 (2000).
- Zelinka, M. D. et al. Causes of higher climate sensitivity in CMIP6 models. *Geophys. Res. Lett.* **47**, e2019GL085782 (2020).
- Kim, H., Kang, S. M., Kay, J. E. & Xie, S.-P. Subtropical clouds key to Southern Ocean teleconnections to the tropical Pacific. *Proc. Natl Acad. Sci. USA* **119**, e2200514119 (2022).
- Hausfather, Z., Marvel, K., Schmidt, G. A., Nielsen-Gammon, J. W. & Zelinka, M. Climate simulations: recognize the 'hot model' problem. *Nature* **605**, 26–29 (2022).
- Sigmond, M. & Fyfe, J. Has the ozone hole contributed to increased Antarctic sea ice extent? *Geophys. Res. Lett.* **37**, L18502 (2010).
- Bitz, C. & Polvani, L. M. Antarctic climate response to stratospheric ozone depletion in a fine resolution ocean climate model. *Geophys. Res. Lett.* **39**, L20705 (2012).
- Ferreira, D., Marshall, J., Bitz, C. M., Solomon, S. & Plumb, A. Antarctic Ocean and sea ice response to ozone depletion: A two-time-scale problem. *J. Clim.* **28**, 1206–1226 (2015).
- Turner, J. et al. Non-annular atmospheric circulation change induced by stratospheric ozone depletion and its role in the recent increase of Antarctic sea ice extent. *Geophys. Res. Lett.* **36**, L08502 (2009).
- Arblaster, J. M. & Meehl, G. A. Contributions of external forcings to southern annular mode trends. *J. Clim.* **19**, 2896–2905 (2006).
- Hall, A. & Visbeck, M. Synchronous variability in the Southern Hemisphere atmosphere, sea ice, and ocean resulting from the annular mode. *J. Clim.* **15**, 3043–3057 (2002).

18. Pauling, A. G., Bitz, C. M., Smith, I. J. & Langhorne, P. J. The response of the Southern Ocean and Antarctic sea ice to freshwater from ice shelves in an Earth system model. *J. Clim.* **29**, 1655–1672 (2016).
19. Haumann, F. A., Gruber, N. & Münnich, M. Sea-ice induced Southern Ocean subsurface warming and surface cooling in a warming climate. *AGU Adv.* **1**, e2019AV000132 (2020).
20. Haumann, F. A., Gruber, N., Münnich, M., Frenger, I. & Kern, S. Sea-ice transport driving Southern Ocean salinity and its recent trends. *Nature* **537**, 89–92 (2016).
21. Purich, A., England, M. H., Cai, W., Sullivan, A. & Durack, P. J. Impacts of broad-scale surface freshening of the Southern Ocean in a coupled climate model. *J. Clim.* **31**, 2613–2632 (2018).
22. Chung, E.-S. et al. Antarctic sea-ice expansion and Southern Ocean cooling linked to tropical variability. *Nat. Clim. Change* **12**, 461–468 (2022).
23. Zhang, L., Delworth, T. L., Cooke, W. & Yang, X. Natural variability of Southern Ocean convection as a driver of observed climate trends. *Nat. Clim. Change* **9**, 59–65 (2019).
24. Li, X., Holland, D. M., Gerber, E. P. & Yoo, C. Impacts of the north and tropical Atlantic Ocean on the Antarctic Peninsula and sea ice. *Nature* **505**, 538–542 (2014).
25. De Lavergne, C., Palter, J. B., Galbraith, E. D., Bernardello, R. & Marinov, I. Cessation of deep convection in the open Southern Ocean under anthropogenic climate change. *Nat. Clim. Change* **4**, 278–282 (2014).
26. Meehl, G. A., Arblaster, J. M., Bitz, C. M., Chung, C. T. & Teng, H. Antarctic sea-ice expansion between 2000 and 2014 driven by tropical Pacific decadal climate variability. *Nat. Geosci.* **9**, 590–595 (2016).
27. Schneider, D. P. & Deser, C. Tropically driven and externally forced patterns of Antarctic sea ice change: Reconciling observed and modeled trends. *Clim. Dyn.* **50**, 4599–4618 (2018).
28. Li, X. et al. Tropical teleconnection impacts on Antarctic climate changes. *Nat. Rev. Earth Environ.* **2**, 680–698 (2021).
29. Watanabe, M., Dufresne, J.-L., Kosaka, Y., Mauritzen, T. & Tatebe, H. Enhanced warming constrained by past trends in equatorial Pacific sea surface temperature gradient. *Nat. Clim. Change* **11**, 33–37 (2021).
30. Jones, J. M. et al. Assessing recent trends in high-latitude Southern Hemisphere surface climate. *Nat. Clim. Change* **6**, 917–926 (2016).
31. Zhang, X., Deser, C. & Sun, L. Is there a tropical response to recent observed Southern Ocean cooling? *Geophys. Res. Lett.* **48**, e2020GL091235 (2021).
32. Kostov, Y. et al. Fast and slow responses of Southern Ocean sea surface temperature to SAM in coupled climate models. *Clim. Dyn.* **48**, 1595–1609 (2017).
33. Plumb, R. A. On the three-dimensional propagation of stationary waves. *J. Atmos. Sci.* **42**, 217–229 (1985).
34. Ding, Q., Steig, E. J., Battisti, D. S. & Wallace, J. M. Influence of the tropics on the southern annular mode. *J. Clim.* **25**, 6330–6348 (2012).
35. Ciasto, L. M., Simpkins, G. R. & England, M. H. Teleconnections between tropical Pacific SST anomalies and extratropical Southern Hemisphere climate. *J. Clim.* **28**, 56–65 (2015).
36. Marshall, G. J. Trends in the Southern Annular Mode from observations and reanalyses. *J. Clim.* **16**, 4134–4143 (2003).
37. Karoly, D. J. Southern hemisphere circulation features associated with El Niño–Southern Oscillation events. *J. Clim.* **2**, 1239–1252 (1989).
38. Trenberth, K. E. et al. Progress during TOGA in understanding and modeling global teleconnections associated with tropical sea surface temperatures. *J. Geophys. Res. Oceans* **103**, 14291–14324 (1998).
39. Folland, C., Renwick, J., Salinger, M. & Mullan, A. Relative influences of the interdecadal Pacific oscillation and ENSO on the South Pacific convergence zone. *Geophys. Res. Lett.* **29**, 21–21–21–24 (2002).
40. Brown, J. R. et al. South Pacific convergence zone dynamics, variability and impacts in a changing climate. *Nat. Rev. Earth Environ.* **1**, 530–543 (2020).
41. Clem, K. R., Lintner, B. R., Broccoli, A. J. & Miller, J. R. Role of the South Pacific convergence zone in West Antarctic decadal climate variability. *Geophys. Res. Lett.* **46**, 6900–6909 (2019).
42. Mo, K. C. & Higgins, R. W. The Pacific–South American modes and tropical convection during the Southern Hemisphere winter. *Mon. Weather Rev.* **126**, 1581–1596 (1998).
43. Newman, M. et al. The Pacific decadal oscillation, revisited. *J. Clim.* **29**, 4399–4427 (2016).
44. Han, W. et al. Intensification of decadal and multidecadal sea level variability in the western tropical Pacific during recent decades. *Clim. Dyn.* **43**, 1357–1379 (2014).
45. Meehl, G. A. et al. Atlantic and Pacific tropics connected by mutually interactive decadal-timescale processes. *Nat. Geosci.* **14**, 36–42 (2021).
46. Ruprich-Robert, Y. et al. Assessing the climate impacts of the observed Atlantic multidecadal variability using the GFDL CM2.1 and NCAR CESM1 global coupled models. *J. Clim.* **30**, 2785–2810 (2017).
47. Yao, S. L., Zhou, W., Jin, F. F. & Zheng, F. North Atlantic as a trigger for Pacific-wide decadal climate change. *Geophys. Res. Lett.* **48**, e2021GL094719 (2021).
48. Simpkins, G. R., McGregor, S., Taschetto, A. S., Ciasto, L. M. & England, M. H. Tropical connections to climatic change in the extratropical Southern Hemisphere: the role of Atlantic SST trends. *J. Clim.* **27**, 4923–4936 (2014).
49. Dong, S., Gille, S. T. & Sprintall, J. An assessment of the Southern Ocean mixed layer heat budget. *J. Clim.* **20**, 4425–4442 (2007).
50. Voldoire, A. et al. Evaluation of CMIP6 deck experiments with CNRM-CM6-1. *J. Adv. Model. Earth Syst.* **11**, 2177–2213 (2019).
51. Boer, G. J. et al. The decadal climate prediction project (DCPP) contribution to CMIP6. *Geosci. Model Dev.* **9**, 3751–3777 (2016).
52. Kang, S. M. et al. Global impacts of recent Southern Ocean cooling. *Proc. Natl Acad. Sci. USA* **120**, e2300881120 (2023).
53. Dong, Y., Armour, K. C., Battisti, D. S. & Blanchard-Wrigglesworth, E. Two-way teleconnections between the Southern Ocean and the tropical Pacific via a dynamic feedback. *J. Clim.* **35**, 6267–6282 (2022).
54. Cai, W. et al. Southern Ocean warming and its climatic impacts. *Sci. Bull.* **68**, 946–960 (2023).
55. Huang, B. et al. Extended reconstructed sea surface temperature version 4 (ERSST.v4). Part I: Upgrades and intercomparisons. *J. Clim.* **28**, 911–930 (2015).
56. Huang, B. et al. Extended reconstructed sea surface temperature, version 5 (ERSSTv5): upgrades, validations, and intercomparisons. *J. Clim.* **30**, 8179–8205 (2017).
57. Hirahara, S., Ishii, M. & Fukuda, Y. Centennial-scale sea surface temperature analysis and its uncertainty. *J. Clim.* **27**, 57–75 (2014).
58. Titchner, H. A. & Rayner, N. A. The Met Office Hadley Centre sea ice and sea surface temperature data set, version 2: 1. Sea ice concentrations. *J. Geophys. Res. Atmos.* **119**, 2864–2889 (2014).
59. Deser, C., Phillips, A. S. & Alexander, M. A. Twentieth century tropical sea surface temperature trends revisited. *Geophys. Res. Lett.* **37** (2010).
60. North, G. R., Bell, T. L., Cahalan, R. F. & Moeng, F. J. Sampling errors in the estimation of empirical orthogonal functions. *Mon. Weather Rev.* **110**, 699–706 (1982).
61. Sen, P. K. Estimates of the regression coefficient based on Kendall's tau. *J. Am. Stat. Assoc.* **63**, 1379–1389 (1968).
62. Bretherton, C. S., Widmann, M., Dymnikov, V. P., Wallace, J. M. & Bladé, I. The effective number of spatial degrees of freedom of a time-varying field. *J. Clim.* **12**, 1990–2009 (1999).
63. Ting, M., Kushnir, Y., Seager, R. & Li, C. Forced and internal twentieth-century SST trends in the North Atlantic. *J. Clim.* **22**, 1469–1481 (2009).

64. Yao, S.-L., Luo, J.-J., Chu, P.-S. & Zheng, F. Decadal variations of Pacific Walker circulation tied to tropical Atlantic–Pacific trans-basin SST gradients. *Environ. Res. Lett.* **18**, 064016 (2023).
65. Boucher, O. et al. Presentation and evaluation of the IPSL-CM6A-LR climate model. *J. Adv. Model. Earth Syst.* **12**, e2019MS002010 (2020).
66. Meehl, G. A. et al. Context for interpreting equilibrium climate sensitivity and transient climate response from the CMIP6 Earth system models. *Sci. Adv.* **6**, eaba1981 (2020).
67. Yao, S.-L., Chu, P.-S., Wu, R. & Zheng, F. Model consistency for the underlying mechanisms for the Inter-decadal Pacific Oscillation–tropical Atlantic connection. *Environ. Res. Lett.* **17**, 124006 (2022).
68. Di Lorenzo, E. et al. ENSO and meridional modes: a null hypothesis for Pacific climate variability. *Geophys. Res. Lett.* **42**, 9440–9448 (2015).
69. Sardeshmukh, P. D. & Hoskins, B. J. The generation of global rotational flow by steady idealized tropical divergence. *J. Atmos. Sci.* **45**, 1228–1251 (1988).

## Acknowledgements

We thank three anonymous reviewers for their constructive comments. This work is supported by the National Science Foundation of China (NSFC42192563 and 42120104001) and the National Key R&D Program for Developing Basic Sciences (2020YFA0608902). We thank Prof. Wenju Cai for the useful discussions and helpful comments that greatly improved this manuscript. We are indebted to the high-performance computing support from Tianhe ([www.nscn-tj.cn](http://www.nscn-tj.cn)), sponsored by the National Supercomputer Center in Tianjin. We acknowledge the World Climate Research Program’s working group on coupled modeling, which led the design of CMIP6 experiments and coordinated the work. We are also grateful to the individual climate modeling group for their efforts in model simulations.

## Author contributions

S.-L.Y. and R.W. conceived the study and wrote the manuscript. S.-L.Y. performed all the data analysis and generated the final figures. J.-J.L. and

W.Z. helped edit the manuscript and refine the results. All authors contributed to interpreting the results and improving this paper.

## Competing interests

The authors declare no competing interests.

## Additional information

**Supplementary information** The online version contains supplementary material available at <https://doi.org/10.1038/s41612-024-00662-w>.

**Correspondence** and requests for materials should be addressed to Shuai-Lei Yao or Renguang Wu.

**Reprints and permissions information** is available at <http://www.nature.com/reprints>

**Publisher’s note** Springer Nature remains neutral with regard to jurisdictional claims in published maps and institutional affiliations.

**Open Access** This article is licensed under a Creative Commons Attribution 4.0 International License, which permits use, sharing, adaptation, distribution and reproduction in any medium or format, as long as you give appropriate credit to the original author(s) and the source, provide a link to the Creative Commons licence, and indicate if changes were made. The images or other third party material in this article are included in the article’s Creative Commons licence, unless indicated otherwise in a credit line to the material. If material is not included in the article’s Creative Commons licence and your intended use is not permitted by statutory regulation or exceeds the permitted use, you will need to obtain permission directly from the copyright holder. To view a copy of this licence, visit <http://creativecommons.org/licenses/by/4.0/>.

© The Author(s) 2024